PUBLISHED BY INSTITUTE OF PHYSICS PUBLISHING AND SISSA

RECEIVED: *January 11, 2006*
ACCEPTED: *February 12, 2006*
PUBLISHED: *April 5, 2006*

DINS measurements on VESUVIO in the Resonance Detector configuration: proton mean kinetic energy in water

Antonino Pietropaolo,[a] Carla Andreani,[b] Alessandra Filabozzi,[b] Roberto Senesi,[b] Giuseppe Gorini,[c] Enrico Perelli-Cippo,[c] Marco Tardocchi,[c] Nigel J. Rhodes[d] and Erik M. Schooneveld[d]

[a] *Consiglio Nazionale delle Ricerche-Istituto Nazionale per la Fisica della Materia UdR Roma Tor Vergata, Via della Ricerca Scientifica 1, 00133, Roma, Italy*
[b] *Università degli Studi di Roma "Tor Vergata", Dipartimento di Fisica Via della Ricerca Scientifica 1, 00133, Roma, Italy*
[c] *Università degli Studi di Milano Bicocca and CNR-INFM Dipartimento di Fisica "G. Occhialini", Piazza della Scienza 2, I-20126 Milano, Italy*
[d] *ISIS Facility, Rutherford Appleton Laboratory Chilton, Didcot, Oxfordshire, OX11 0QX, U.K.*
E-mail: pietropaolo@roma2.infn.it, andreani@roma2.infn.it, filabozzi@roma2.infn.it, senesi@roma2.infn.it, gorini@mib.infn.it, perelli@mib.infn.it, tardocchi@mib.infn.it, N.J.Rhodes@rl.ac.uk, E.M.Schooneveld@rl.ac.uk

ABSTRACT: Deep Inelastic Neutron Scattering (DINS) measurements have been performed on a liquid water sample at two different temperatures and pressures. The experiments were carried out using the VESUVIO spectrometer at the ISIS spallation neutron source. This experiment represents the first DINS measurement from water using the Resonance Detector configuration, employing yttrium-aluminum-perovskite scintillator and a ^{238}U analyzer foil. The maximum energy of the scattered neutrons was about 70 eV, allowing to access an extended kinematic space with energy and wave vector transfers at the proton recoil peak in the range 1 eV $\leq \hbar\omega \leq$ 20 eV and 25 Å$^{-1} \leq q \leq$ 90 Å^{-1}, respectively. Comparison with DINS measurements on water performed in the standard Resonance Filter configuration indicates the potential advantages offered by the use of Resonance Detector approach for DINS measurements at forward scattering angles.

KEYWORDS: Instrumentation for neutron sources; Gamma detectors (scintillators, CZT, HPG, HgI etc).

2006 JINST 1 P04001

Contents

1. Introduction

The Resonance Detector (RD) [1 – 4] is a neutron detection method recently developed on VESUVIO at the ISIS spallation neutron source [5]. VESUVIO is an inverse geometry time of flight spectrometer where a "white" neutron beam is scattered off a sample and the scattering process is reconstructed by recording both final energy and time of flight of the scattered neutrons. Neutron detection in the RD configuration is performed in a two-step process: an analyzer foil — exploiting the (n,γ) resonance reactions occurring in selected isotopes such as ^{238}U or ^{197}Au — is used for converting neutrons into γ's, and these are recorded with yttrium-aluminum-perovskite (YAP) scintillators or cadmium-zinc-telluride (CZT) semiconductor detectors. Thanks to this combination of analyzers and detectors [6, 7], neutrons up to final energies of about 70 eV have been measured successfully on VESUVIO.

In this paper we report on the first use of the RD method for Deep Inelastic Neutron Scattering (DINS) measurements on liquid water at two different thermodynamic conditions. The RD measurements were carried out parasitically in parallel to measurements performed with a Resonance Filter (RF) set up on VESUVIO [8]. In the RF configuration, which is the standard on the instrument, the neutron time of flight (TOF) is recorded using ^{6}Li-glass scintillators as neutron detectors; the final neutron energy is selected by neutron resonance absorption in an analyzer filter, while the scattering signal is provided by the difference between two independent measurements with and without the analyzer (i.e. ^{197}Au in the present experiment). The RD measurements on liquid water presented in this paper were meant to develop a specific data analysis in order to extract useful physical information from the RD data and to demonstrate the potential of the RD approach when

2006 JINST 1 P04001

compared to the RF measurements. In particular the RD measurements reported in this experimental work on a water sample are the first of this kind. The experiment has been performed in a range of final neutron energies, E_1, up to a value of E_1 of about 70 eV, not accessible on VESUVIO when operated with the RF configuration. In fact the ^{6}Li-glass neutron counters used on VESUVIO in the RF configuration suffer of heavy detection efficiency losses and low signal to background ratio for final neutron energies above 10 eV [6], thus limiting the energy range for their effective use in DINS measurements.

These measurements demonstrate that, using the RD method, it is possible to access a kinematical $(q, \hbar\omega)$ region corresponding to 1 eV $\leq \hbar\omega \leq$ 20 eV and 25 Å$^{-1} \leq q \leq$ 90 Å^{-1}, at the proton recoil peak, with a single fixed-angle detector. The kinematical space will be further extended when RD detector arrays covering a broad angular range will become available.

2. Experiment and data analysis

Figure 1 shows a schematic layout of the experimental set up for the RF and RD measurements on VESUVIO. In the figure *n* is the incident neutron beam. The sample, placed inside an aluminium vacuum chamber, was at a distance $L_0 \simeq 11$ m from the water moderator.

The ^{6}Li-glass detector banks for the RF measurements, namely A, B, C and D, were equipped with a total of 32 scintillating elements, each coupled to a photomultiplier tube, covering the angular range 30°-70°. The average distance of the ^{6}Li-glass detectors from the sample was about $L_1 \simeq 0.7$ m. The ^{197}Au analyzer foils, placed between the sample and the detectors, were at an average distance from the ^{6}Li-glass detectors of about 0.35 m.

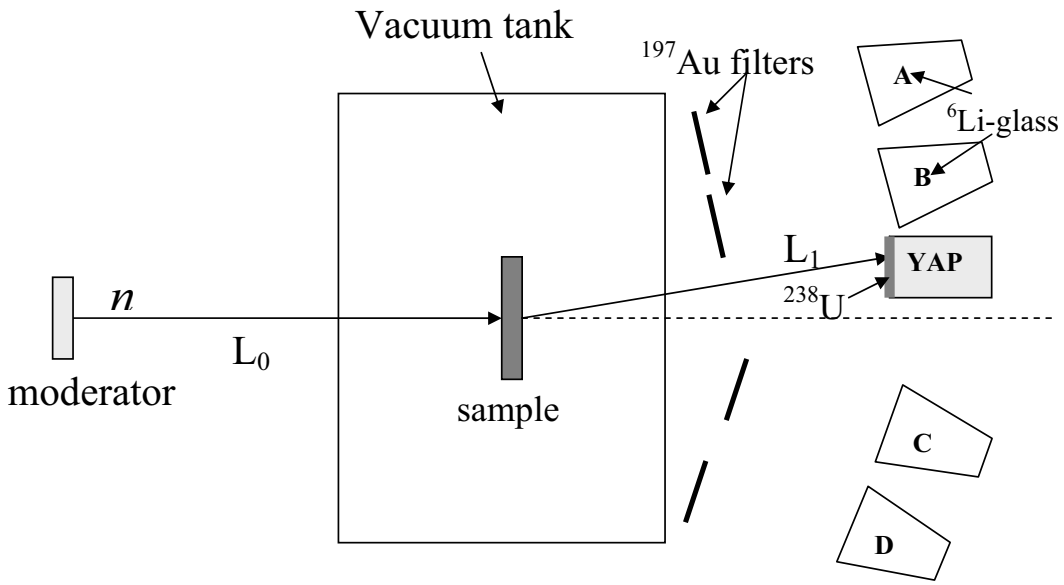

Figure 1. A schematic view of the VESUVIO spectrometer showing the set up of the DINS experiment on liquid water, in both RF and RD configurations. In RF and RD measurements, scattered neutrons are recorded by the ^{6}Li neutron detectors (banks A,B,C,D) and by the YAP γ detectors, respectively.

Isotope	E_1 (eV)	σ_0 (b)	Γ_0 (meV)
^{238}U	6.67	23564	25
^{238}U	20.8	37966	34
^{238}U	36.6	42228	57
^{238}U	66.0	20134	48

Table 1. Physical parameters of the nuclear resonances for the ^{238}U analyzer foil used for the RD configuration: E_1 is the resonance energy of the analyzer foil, σ_0 is the resonance cross section at peak position and Γ_0 is the resonance intrinsic Lorentzian width.

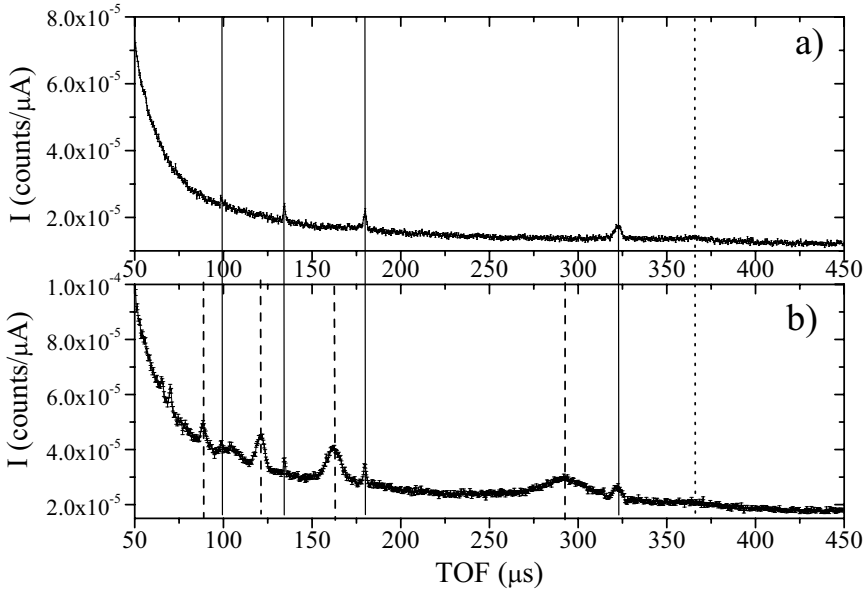

Figure 2. Time of flight DINS spectra from (a) Al empty container and (b) water sample at T=293 K and p=1 bar. Vertical continuous, dashed and dotted lines indicate, respectively, the positions of the recoil peak from ^{27}Al and ^{16}O atoms, of the H recoil peaks and of the container recoil peak due to neutrons scattered off the cell and absorbed, at the energy E_1=4.906 eV, by the ^{197}Au analyzer foils, used for the RF measurements.

The detector for the RD measurements was placed close to the ^{6}Li-glass detector bank B (see figure 1) at a scattering angle $2\theta \simeq 27^\circ$ and at the same distance L_1 from the sample. It was made of a cylindrical YAP scintillator (3.5 cm diameter and 6 mm thick) combined with a ^{238}U analyzer foil of (3.5 x 3.5) cm^2 area and 30 μm thickness. The physical parameters of the nuclear resonances for the ^{238}U analyzer foil are listed in table 1. Data were acquired with a Lower Level Discrimination (LLD) threshold corresponding to about 50 keV equivalent γ energy. This setting allows the calibration of the angular position of the RD modulus using a cadmium analyzer (see below).

DINS measurements were performed on liquid water below the critical point, at two different thermodynamic $[p,T]$ conditions, namely [1 bar, 293 K] and [100 bar, 423 K], at VESUVIO using both the RF and RD configurations. Two different sample containers have been used for the measurements: an aluminum (Al) sample container for the experiments at [1 bar, 293 K] and a

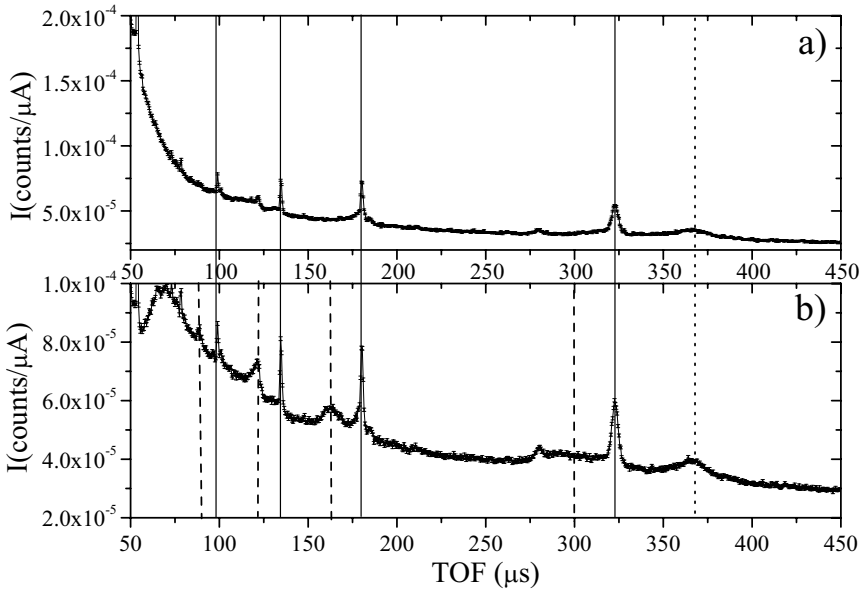

Figure 3. Time of flight DINS spectrum from TiZr empty container (a) and water sample at T=293 K and p=1 bar (b). Vertical continuous, dashed and dotted lines, respectively, indicate the positions of the recoil peak from ^{48}Ti, ^{91}Zr and ^{16}O atoms, of the H recoil peaks and of the container recoil peak due to neutrons scattered off the cell and absorbed, at the energy E_1=4.906 eV, by the ^{197}Au analyzer foils, used for the RF measurements.

titanium-zirconium (TiZr) container for the experiments at [1 bar, 293 K] and [100 bar, 423 K]. The experimental signal recorded by the γ detector is a time of flight spectrum. It represents the number of counts collected in a time channel of width δt centered in t. Figures 2, 3 and 4 show examples of the normalized time of flight DINS spectra of water in Al and TiZr containers in the experimental region 50 μs - 450 μs. The top diagram in each figure represents the scattering spectrum from the empty container which provides a direct measurement of part of the background; the bottom diagram is the time of flight DINS spectrum of water and container. In figures 2 and, 3 and 4, vertical continuous lines at 100 μs, 130 μs, 180 μs and 320 μs identify the position of the recoil peaks of the ^{27}Al and ^{16}O and ^{48}Ti, ^{91}Zr and ^{16}O nuclei, respectively. Each line corresponds to distinct values of the final neutron energy, E_1, of the ^{238}U analyzer foil (see table 1). In all figures vertical dashed lines, at 90 μs, 124 μs, 160 μs and 290 μs, identify the positions of the H recoil peaks at distinct values of the resonance energies E_1. In figures 3(b) and 4(b) the broad peak at about 70 μs can be ascribed to signal saturation mechanisms in the data acquisition electronics, due to the high count rate from the H_2O in the TiZr sample container. Indeed this feature is not present in data from water in Al sample container (see figure 2(b)), where the scattering power is smaller as compared to TiZr alloy.

In order to derive the DINS spectra of the H recoil peaks, the background and the sample container components need to be subtracted from the experimental time of flight spectra. The background signal is composed of a continuum, which can be fitted and subtracted from the data (see below), and by peaks, such as those due to neutrons scattered off the walls of the Al and TiZr containers. In the latter case some of the peaks are specific of the parasitic conditions of this present

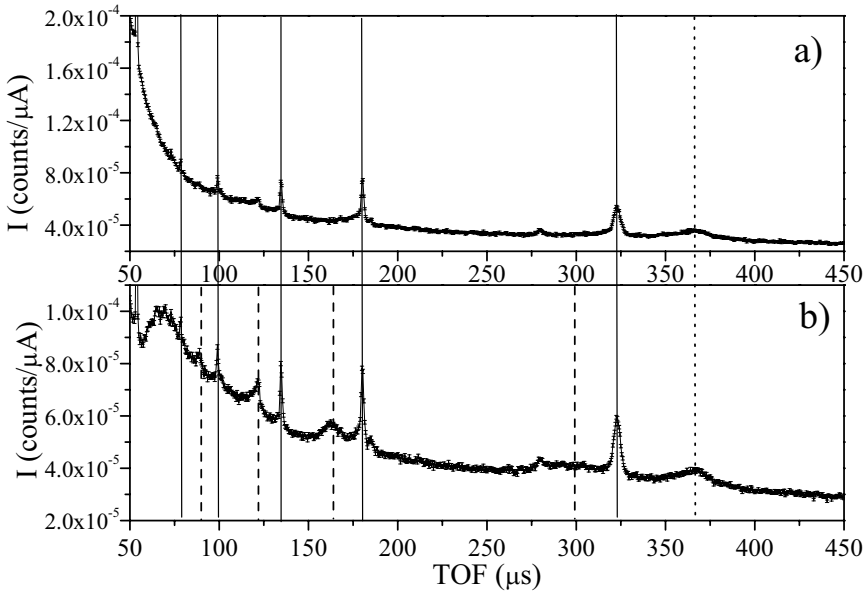

Figure 4. Time of flight DINS spectra from TiZr empty container (a) and water sample at T=423 K and p=100 bar (b). Vertical continuous, dashed and dotted lines indicate the positions of the recoil peak from ^{48}Ti, ^{91}Zr and ^{16}O atoms, of the H recoil peaks and of the container recoil peak due to neutrons scattered off the cell and absorbed, at the energy E_1=4.906 eV, by the ^{197}Au analyzer foils, used for the RF measurements.

RD configuration and therefore not intrinsic of the RD method. An example is represented by the broad peaks in figures 2, 3 and 4 marked with vertical dotted lines at a time of flight value of about 365 μs. These peaks, recorded by the γ detectors in the RD measurements, are associated to those neutrons which scattered off the sample container and are absorbed, at the energy E_1=4.906 eV, in the ^{197}Au foils in front of the ^{6}Li scintillators used for the RF measurements. This description is consistent with the time delay, Δt, observed in figure 5 between the positions of the absorption dip recorded by the ^{6}Li-glass detector bank B, close to the YAP γ detector (lower plot), and the peak observed in the RD spectra (upper plot). This time delay (about 12 μs) is the time it takes a 4.906 eV neutron to travel the distance of 0.35 m between the ^{197}Au filter and the ^{6}Li-glass detector. The peak is weak and less pronounced in figure 2 as compared to those in figures 3 and 4 because of the lower scattering power of the Al sample container as compared to the TiZr. Another peak component in the background signal comes from neutrons scattered off the H atoms in the sample and absorbed in the ^{197}Au analyzer foils. The result of this can be appreciated from figure 6 which shows the time of flight DINS spectra from water in the Al container, in RD (upper plot) and RF (lower plot) configurations. In figure 6(b) the dip, centered at about 330 μs, is the H recoil signal corresponding to the final neutron energy E_1=4.906 eV of the ^{197}Au analyzer foil in front of the ^{6}Li detector bank B (se figure 1). In figure 6(a) the peak at about 290 μs represents the H recoil signal, corresponding to a final neutron energy E_1=6.671 eV of the ^{238}U analyzer foil in front of the YAP detector. In analogy with the observation of figure 5 we are led to believe that their must be some contamination of the RD spectrum that is correlated with the dip in the RF spectrum. More precisely, the time interval within the dashed lines of figure 6 where the two signals overlap may be

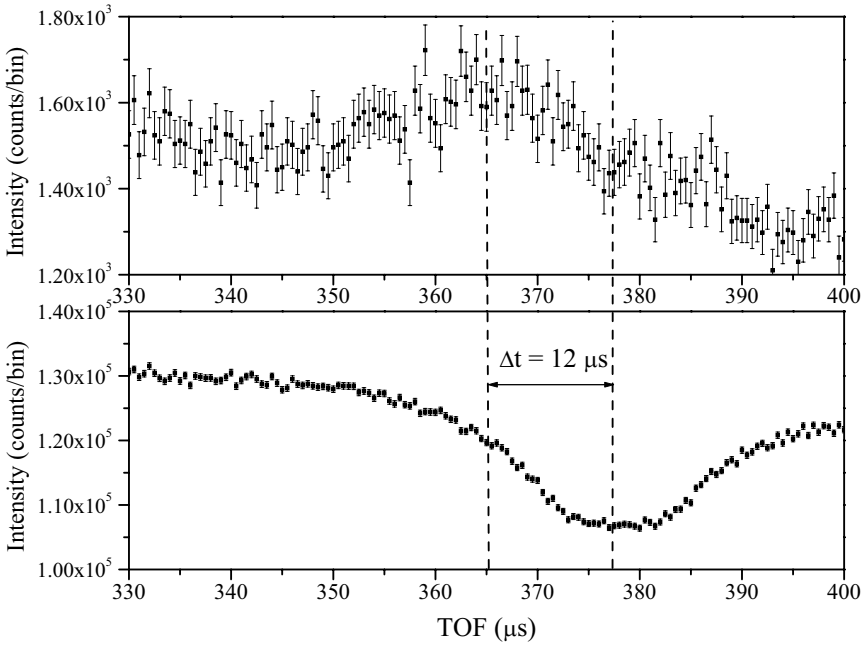

Figure 5. Time of flight DINS spectra in the 330 μs - 400 μs region from the empty TiZr sample container recorded in the RD (upper plot) and the RF (lower plot) configurations, using the YAP γ detector and the closest ^{6}Li scintillator, respectively. The time delay, Δt=12 μs, is the time for a 4.906 eV neutron to travel the distance between the ^{197}Au filter and the ^{6}Li-glass detector.

contaminated by background. This contamination can be easily avoided in a dedicated experiment by removing the gold foils; for the present parasitic measurements the only way to deal with this background component was to exclude the contaminated recoil peaks from the analysis.

A further step in the data reduction is to remove in the water spectrum the signal coming from the sample containers, i.e. (a) spectra from the (b) spectra in figures 2-4. In the difference spectra the container dependent background is removed with quite good accuracy. Results for the water data in Al container are shown in figure 7. The shape of the signal in between the H recoil peaks can be used to interpolate the background underneath the peaks. In the time intervals between the peaks, the residual background has been fitted by an appropriate function [9]. The fitted function is shown, as a full line, in figure 7. Subtraction of the fitted background continuum leads to the time of flight spectrum shown in figure 8. The same procedure has been applied to the whole set of time of flight spectra. This approach is not entirely free from systematic uncertainties (*e.g.* due to the broad gold contamination peaks hiding beneath the H recoil peaks) and one of the purposes of this work is to show that it leads to results consistent with those obtained from DINS measurements in the RF configurations.

A background source deserving special attention occurs in the form of peaks due to (n,γ) resonance absorption reactions most likely occurring in the sample container's surrounding device, such as the furnace employed in the TiZr measurements, or in contaminants present in the container itself. Figure 9 shows an expanded view of the TOF spectra in the case of TiZr sample container at room temperature (full, empty and subtraction of the two) in the time interval 100 μs - 350 μs.

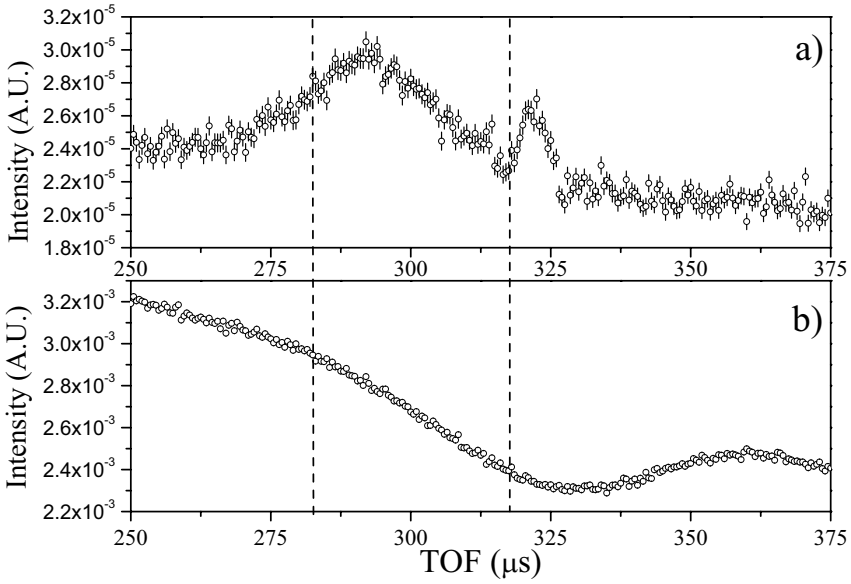

Figure 6. Time of flight spectra from water sample at [1 bar, 293 K] in the Al container recorded in the RD configuration (a) and in the RF configuration (from ^{6}Li-glass detector bank B) (b). The dashed lines limit the time of flight region where radiative capture γ's, from the ^{197}Au analyzer foil contaminate the H recoil spectrum recorded by the YAP γ detectors. The peak at about 320 μs is the recoil peak from ^{27}Al and ^{16}O atoms in the sample container.

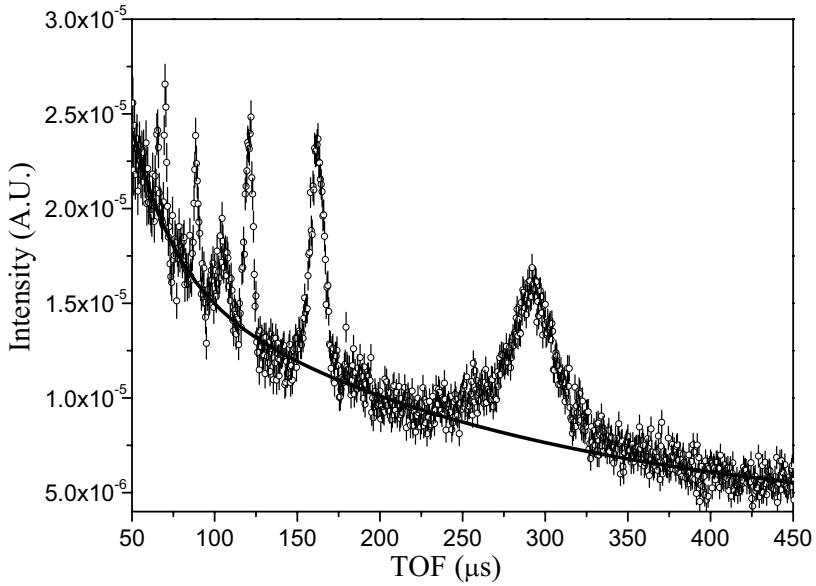

Figure 7. Time of flight DINS spectrum of water at T=293 K and p=1 bar, obtained from the difference of the spectra of figure 2. The continuous line represents the background fitted to the experimental data.

The four peaks labeled γ_1-γ_4 are most likely induced by neutron resonance absorption in different elements. The well defined time position of the peaks allowed for an estimation of the resonance

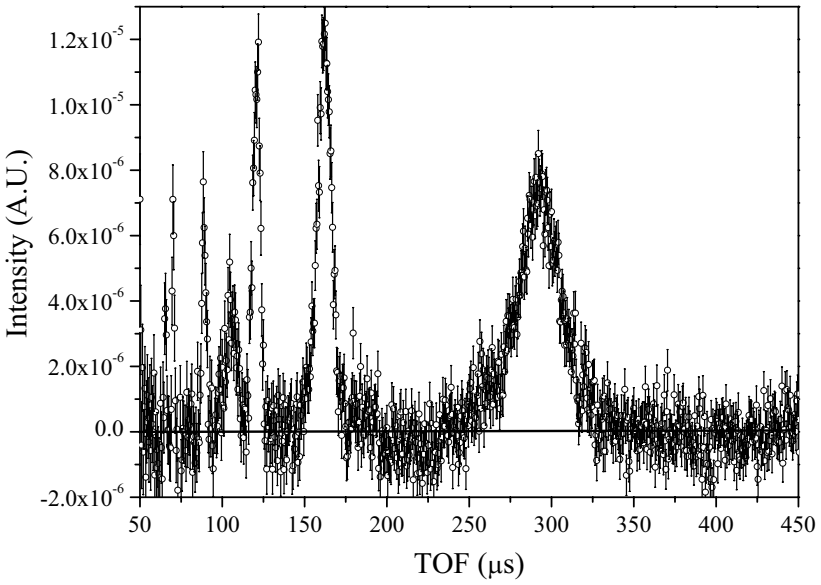

Figure 8. Time of flight DINS spectrum of water at T=293 K and p=1 bar, with background removed.

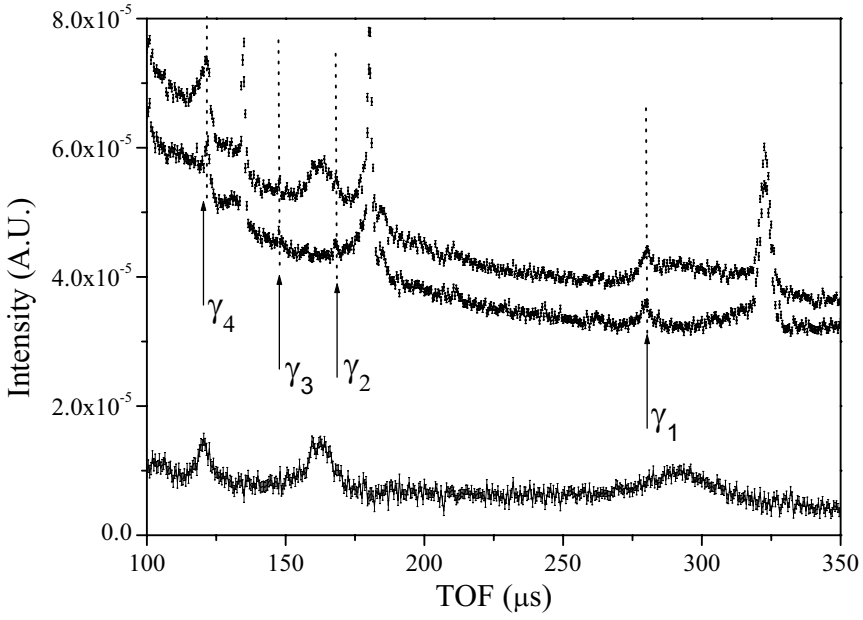

Figure 9. From top to bottom: time of flight spectra of water at [1 bar, 293 K] in TiZr container, empty TiZr container and difference spectrum. Vertical lines mark the peaks induced by the radiative capture γ's from sample container environment.

energy of the possible contaminants in the furnace/container. The possible elements are ^{183}W (E_1 7.6 eV), ^{123}Sb (E_1 = 21.4 eV) as well as different isotopes of ^{150}Sm (E_1 = 20.7 eV, 39.4 eV).

The problem with these peaks is that, depending on sample and container thickness, they may not cancel exactly in the difference spectrum. In the future the problem can be mitigated by noting

that the radiative capture γ lines with high relative intensity of these isotopes are found in the low energy region (say below 500-600 keV). Thus their intensity can be effectively suppressed by using a high LLD threshold [7]. For the present experiment, where a low LLD threshold was used, there can be an effect especially if the spurious peaks are located beneath an H signal peak. In particular:

- the (n,γ) peak γ_1, placed at about 285 μs, is superimposed to the first H recoil peak. Thus it could increase its apparent width together with the gold foil contribution discussed in figure 5;
- the γ_2 peak at about 170 μs is placed on the tail of the second H signal peak and should not provide significant broadening contribution;
- the γ_3 peak at about 150 μs is in between the second and third H signal peaks and presents no problem;
- the γ_4 peak at about 125 μs is right on the third H signal peak.

If $\rho_{\gamma,j}$ (j = 1,2,3,4) is the peak to background ratio for the *j-th* (n,γ) peak in the empty can spectrum, the values $\rho_{\gamma,1}$ = 0.13, $\rho_{\gamma,2}$ 0.04 and $\rho_{\gamma,4}$ = 0.09 are found. This means that the (n,γ) spurious contamination should be much more important for the first and third H signal peaks rather than for the second one in the TiZr measurements.

3. Calibrations

The analysis of the H recoil spectra requires independent knowledge of a number of instrumental parameters. Some of these parameters have been experimentally determined or "calibrated", namely the secondary flight path L_1, the time delay t_0 and the scattering angle 2ϑ.

As the experimental calibration procedure of a RD spectrometer is slightly different from that applied in the RF configuration, a detailed description of the main steps is presented in the following.

As far as the primary flight path, L_0 and the final energy, E_i ($i = 1,2,3$ indexing the distinct ^{238}U resonances, see table 1) we have used values calibrated from previous experiments [10]. The total flight path $(L_0 + L_1)$ for the YAP detector has been determined from the position in time of flight of the recoil peaks due to scattering off the aluminum sample container. For free recoil scattering processes, the change in neutron velocity is determined only by the conservation on kinetic energy and wave vector. Hence, the ratio of the final neutron velocity, v_1, to the initial one, v_0, is a function of ϑ and of the atomic mass M and can be written as:

$$\frac{v_1}{v_0} = F(\vartheta) = \frac{\cos 2\vartheta + \sqrt{(\frac{M}{m})^2 - \sin^2 2\vartheta}}{\frac{M}{m} + 1} \tag{3.1}$$

while the time of flight is given by [10]:

$$t = t_0 + [L_0 F(\vartheta) + L_1]\frac{1}{v_1} \tag{3.2}$$

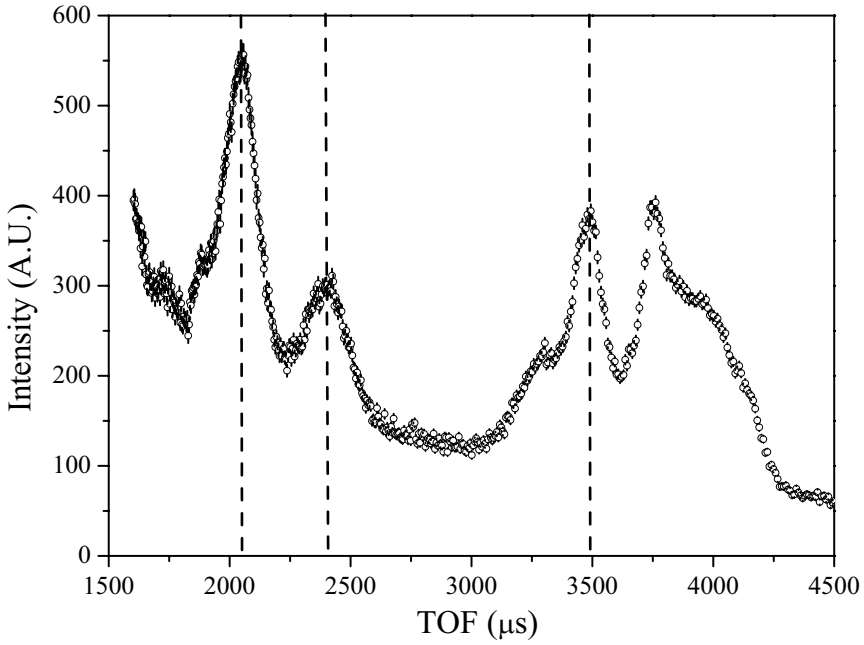

Figure 10. Diffraction pattern of Pb acquired with the YAP detector recording the γ's from neutron absorption in a 1 mm thick cadmium analyzer foil. The dashed lines indicate the diffraction peaks corresponding to the set of planar distances d and Miller indexes [hlm] listed in table 2.

t_0 being an instrumental (electronics) offset. The coefficients $L_0F(\vartheta)+L_1$ and t_0 can be determined by fitting the linear relation (3.2) to the t and $\frac{1}{v_1}$ data, which are known for each of the four Al scattering peaks. The fit procedure yields the values for L_1 and t_0 needed for the analysis.

Independent experimental information is required for angle calibration. The two step method used here consisted in: (a) replacing the ^{238}U foil in front of the YAP scintillator with a ^{113}Cd analyzer foil (1 mm thickness), a well known absorber of thermal neutrons up to about 400 meV; (b) measuring the time of flight spectrum from a Pb sample. The strongest prompt γ emission peak of ^{113}Cd is at 558.5 keV so that these photons were recorded by the YAP scintillator setting a sufficiently low value for γ energy discrimination, i.e. a threshold at 50 keV. In the thermal energy range of the spectrum the position in time of flight of the Bragg diffraction peaks from Pb (see figure 10) yields the angular position of the Cd foil. Bragg peaks are present in a spectrum recorded by a detector placed at angle 2ϑ if the relation:

$$2d\sin\vartheta = n\lambda \tag{3.3}$$

is satisfied, with

$$\lambda = \frac{\hbar}{mv} \tag{3.4}$$

being de Broglie neutron wavelength, d is the spacing between two subsequent planes, and n an integer. Bragg scattering is elastic, i.e. $v_0 = v_1 = v$. Therefore v is given by

$$v = \frac{L_0 + L_1}{t - t_0} \tag{3.5}$$

Using equations (3.3) and (3.5), a relationship between the scattering angle and the measured time

TOF (μs)	d (Å)	[hlm]
2045	1.489	[311]
2403	1.750	[220]
3491	2.475	[200]

Table 2. Time positions, d-spacing and corresponding Miller indexes [hlm] for the Bragg peaks in the diffraction pattern shown in figure 10.

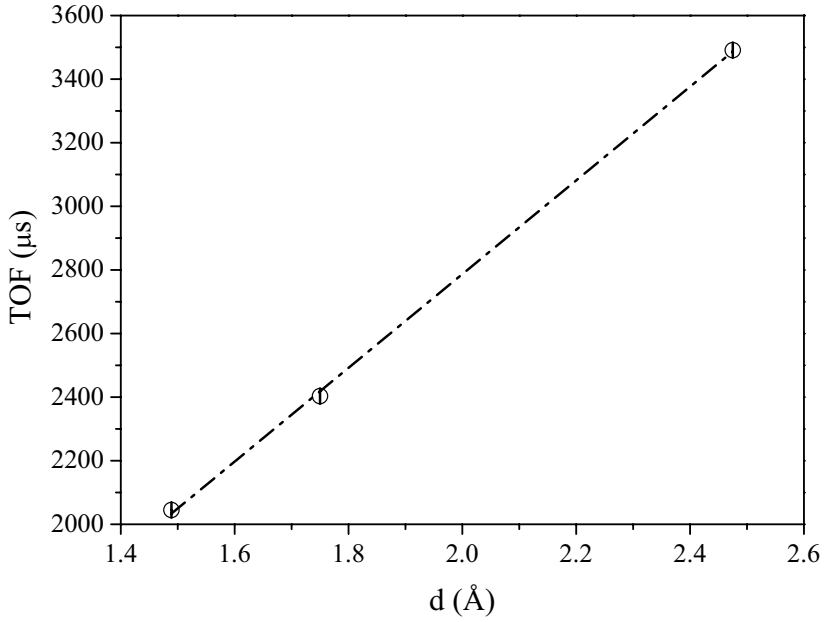

Figure 11. Plot of the d-spacing versus neutron TOF and corresponding linear fit used for the calibration of the RD angular position.

of flight at which Bragg peaks from Pb occur can be obtained:

$$2d\sin\vartheta = \frac{n\bar{h}(t-t_0)}{m(L_0+L_1)}\,. \tag{3.6}$$

Thus by plotting the time positions of the Bragg peaks against d and performing a least squares fit, a slope value is obtained which is proportional to $\sin\vartheta$. Figure 11 shows the linear fit to the experimental data (d vs TOF). The experimental points chosen for the fit are those corresponding to the peaks located at about 2045 μs, 2403 μs and 3491 μs, which can be unambiguously ascribed to a given set of d-spacings and Miller indexes [hlm], as shown in table 2. The unidentified peak located at about t=3750 μs in figure 10 may be contributed by some impurity in the lead sample and was not included in the fit. The angle calibration is based on independent knowledge of L_1 from the flight path calibration which, however, requires independent knowledge of the detector angle. Thus the two calibration methods were combined in an iterative procedure until convergence on a consistent set of 2ϑ, L_1 and t_0 values was reached. The calibrated values of the instrumental parameters derived by this procedure are reported in table 3.

parameter	value
L_0	(11.055 $\pm$ 0.021) m
L_1	(0.685 $\pm$ 0.020) m
2ϑ	(26.7 $\pm$ 2.0)$^\circ$
t_0	(-4.95 $\pm$ 0.30) μs
E_1	(6.677 $\pm$ 0.053) eV
E_2	(20.878 $\pm$ 0.095) eV
E_3	(36.688 $\pm$ 0.142) eV

Table 3. Calibrated instrumental parameters.

4. Analysis

The H signal peaks derived from the measured time of flight spectra can be analyzed to yield the single particle dynamics of the H nuclei in the sample within the framework of the Impulse Approximation (IA) [11]. The inelastic neutron scattering cross-section for unpolarized neutrons is related to the dynamic structure factor S($\mathbf{q}, \omega$) via the relation [12, 13]:

$$\frac{d^2\sigma(E_0, E_1, 2\vartheta)}{d\Omega dE_1} = \hbar^{-1}\sqrt{\frac{E_1}{E_0}}\left[|b|^2 S(\mathbf{q},\omega) + (|b^2| - |b|^2) S_I(\mathbf{q},\omega)\right] \tag{4.1}$$

where b is the scattering length, E_1 the energy of the scattered neutron, E_0 that of the incident neutron and 2ϑ is the scattering angle. At the high q values in the experiments, the scattering is entirely incoherent, that is it occurs from single particle. The interpretation of DINS data relies essentially on the fact that, provided the momentum $\hbar q$ transferred between the incident neutron and the target system is sufficiently high, the inelastic neutron scattering cross-section provides a direct probe of the distribution of atomic momenta in the target system. Within the framework of the IA, the inelastic neutron scattering cross-section in equation (4.1) is:

$$\frac{d^2\sigma(E_0, E_1, 2\vartheta)}{d\Omega dE_1} = \hbar^{-1}\sqrt{\frac{E_1}{E_0}}\left[|b^2| S_{IA}(\mathbf{q},\omega)\right] \tag{4.2}$$

where

$$S_{IA}(\mathbf{q},\omega) = \hbar \int n(\mathbf{p})\ \delta\left[\hbar\omega - \hbar\omega_r - \frac{\mathbf{p}\cdot\hbar\mathbf{q}}{M}\right] d\mathbf{p} \tag{4.3}$$

In equation (4.3) $\hbar\omega_r$ is the *recoil energy*:

$$\hbar\omega_r = \frac{\hbar^2 q^2}{2M} \tag{4.4}$$

The physical implication of equation (4.3) is that scattering occurs between the neutron and a single particle, with conservation of kinetic energy and momentum of the particle+neutron system. The term $\hbar\omega_r$ is the kinetic energy the struck particle would have, providing it were stationary and absorbed all the momentum transferred by the neutron. It gives the center of the observed peak at a given q associated with the particle of mass M. The momentum distribution of the struck particles broadens this line by a similar mechanism to the Doppler broadening of spectral lines by

atomic motions. Since the position depends on M, different mass particles in the sample can be distinguished in the observed spectrum.

If the IA is valid the two dynamic variables, ω and q, can be explicitly coupled through the definition of the scaling variable y as [12]:

$$y = \frac{M}{\hbar^2 q}\left(\hbar\omega - \hbar\omega_r\right) \tag{4.5}$$

Equation (4.3) can then be reduced to the form

$$S_{IA}(\mathbf{q},\omega) = \frac{M}{\hbar q} J(y,\hat{q}) \tag{4.6}$$

where

$$J(y,\hat{q}) = \hbar \int n(\mathbf{p}')\ \delta(\hbar y - \mathbf{p}'\cdot\hat{q})\ d\mathbf{p}' \tag{4.7}$$

$J(y,\hat{q})$ is the *Neutron Compton Profile* and is formally the Radon transform of the momentum distribution. The quantity $\hat{q}$ is a unit vector, as $J(y,\hat{q})$ no longer depends on the magnitude of $\mathbf{q}$. The function $J(y,\hat{q})dy$ (sometimes also indicated as $F(y,\hat{q})dy$ in the literature) is physically the probability for an atom to have a momentum parallel to $\hat{q}$ of a magnitude between $\hbar y$ and $\hbar(y+dy)$.

In an isotropic system, the direction $\hat{q}$ is immaterial, and equation (4.7) becomes

$$J(y) = 2\pi\hbar \int_{|\hbar y|}^{\infty} p\, n(p)\, dp \tag{4.8}$$

The single-particle mean kinetic energy, $\langle E_K \rangle$, is related to the second moment of $J(y)$ via:

$$\int_{-\infty}^{\infty} y^2 J(y)\, dy = \sigma_y^2 = \frac{2M}{3\hbar^2}\langle E_K \rangle \tag{4.9}$$

where σ_y is the standard deviation of the Neutron Compton Profile.

The standard expression for the number of neutrons detected in time channel t in an inverse geometry spectrometer is: [14]:

$$C(t) = 2\hbar \left[\frac{2}{m}\right]^{\frac{1}{2}} \frac{E_0^{3/2}}{L_0} I(E_0) D(E_1) N \frac{d^2\sigma}{d\Omega dE_1}\, d\Omega \tag{4.10}$$

where $I(E_0)\, dE_0$ is the number of neutrons incident with energies between E_0 and $E_0 + dE_0$, $D(E_1)$ is the probability that a neutron of energy E_1 is detected, N is the number of atoms in the beam and $d\Omega$ is the solid angle subtended by the detector. The count rate can be expressed in terms of the Neutron Compton Profile as:

$$C_M(t) = \frac{E_0 I(E_0)}{\hbar^2 q} A_M M J_M(y_M) \tag{4.11}$$

where:

$$A_M = \frac{2}{L_0} D(E_1) \sqrt{\frac{2E_1}{m}} d\Omega\, N_M b_M^2 \tag{4.12}$$

with $J_M(y_M)$ being the Neutron Compton Profile for mass M and y_M is given by equation (4.5). A basic assumption of the IA is that the scattering is incoherent, hence if there are a number of

different masses present in the sample the overall count rate is simply obtained by summing the contribution from atoms of different mass. The count rate is then:

$$C(t) = \sum_M C_M(t) = \frac{E_0 I(E_0)}{\hbar^2 q} \sum_M A_M M J_M(y_M) \tag{4.13}$$

In the derivation of equation (4.13) it is assumed that the *instrument parameters* $L_0, L_1, 2\theta$ and E_1 are known exactly. In reality these quantities can be assessed only according to some probability distribution $P(L_0, L_1, 2\theta, E_1)$, which determines the instrument resolution. The measured count rate, $C_m(t)$, is an average over the possible values of these parameters, weighted by their probability of occurrence:

$$C_m(t) = \int C_M(t) P(L_0, L_1, 2\vartheta, E_1)\, dL_0\, dL_1\, d\vartheta\, dE_1 \tag{4.14}$$

The exact incorporation of the instrument resolution function would entail the evaluation of this four dimensional integral for each data point, in addition to the convolution in t, required to incorporate the uncertainty in the measurement of the time of flight. To reduce data processing times, the Convolution Approximation is assumed in the data analysis, i.e. the resolution is incorporated as a single convolution in t space, with a mass dependent resolution function, $R_M(y)$. Thus equation (4.13) is modified to:

$$C_m(t) = \frac{E_0\, I(E_0)}{\hbar^2 q} \sum_M A_M\, M\, J_M(y_M) \otimes R_M(y) \tag{4.15}$$

It is worthwhile mentioning that the IA is strictly valid only in the asymptotic double limit $q \to \infty$, $\omega \to \infty$, keeping y constant. For finite values of the energy and wave vector transfers, the longitudinal momentum distribution retains an additional dependence on q which is known as Final State Effect (FSE). A detailed description of this contribution can be found in references [15, 16].

5. Results

The time of flight spectra of water at each thermodynamic state show four main recoil proton peaks (see for examples figures 7 and 8), corresponding to the four resonances of the ^{238}U analyzer (see table 1). Thus the time of flight spectra, transformed in y space within the framework of the IA according to equation (4.5), provide four corresponding response functions, $F(y)$, namely the experimental Neutron Compton Profiles. Due to the poor statistics, the recoil peak corresponding to a final neutron energy of 66 eV (fourth ^{238}U resonance) has not been considered for further analysis. A total of nine experimental response functions $F(y)$ have been analyzed: six $F(y)$ for the room temperature sample (for the Al and TiZr containers) and three for the higher temperature one (for the TiZr container). Each group of spectra has been fitted simultaneously using a minimization procedure based on the MINUIT package [17]. The fitting procedure employed a single Neutron Compton Profile of the proton in the molecular system under study, $J(y)$, convoluted with the resolution function $R_i(y)$, corresponding to the specific final energy. Generally speaking the resolution function is a convolution of a Gaussian and a Lorentzian lineshapes: the first component describes contributions due to the uncertainties on the geometrical parameters (L_0, L_1, 2ϑ), the time of flight

2006 JINST 1 P04001

t and the Doppler component of the resonance absorption cross section; the Lorentzian component is due to the intrinsic single nucleus (Breit-Wigner) resonance cross section. Thus the experimental response functions, $F_i(y)$ can be formally written as:

$$F_i(y) = J(y) \otimes R_i(y) \ , \tag{5.1}$$

where $J(y)$ does not depend on the value of the index (i is the resonance index defined in section 3).

In order to compare the results obtained with the two spectrometer configurations the $J(y)$ has been fitted using different models for the proton momentum distribution. The isotropic Gaussian model, the simplest model to use in the fitting procedure, yields:

$$J(y) = \frac{1}{\sqrt{2\pi}\sigma} \cdot \exp^{-\frac{y^2}{2\sigma^2}} \tag{5.2}$$

where σ is related to the mean kinetic energy by the relation:

$$\langle E_K \rangle = \frac{3}{2m}\bar{h}^2\sigma \tag{5.3}$$

Previous DINS work performed on non-hydrogen bonded and hydrogen bonded systems has clearly demonstrated that it is only a crude model which does not fully account for the physical characteristics of the proton dynamics [18 – 21]. A more sophisticated model, which better describes the proton dynamics in the case of supercritical H_2O [19] and solid H_2S [18], is the anisotropic Gaussian model for the proton momentum distribution, where $J(y)$ is given by [18]:

$$J(y) = \int_{-1}^{1} d(cos\vartheta) \frac{(\frac{cos^2\vartheta}{\sigma^2(\widehat{z})} + \frac{sin^2\vartheta}{\sigma^2(\widehat{t})})^{-1}}{\sqrt{2\pi}\sigma^2(\widehat{t})\sigma^2(\widehat{z})} \exp\left[-\frac{y^2}{2}\left(\frac{cos^2\vartheta}{\sigma^2(\widehat{z})} + \frac{sin^2\vartheta}{\sigma^2(\widehat{t})}\right)\right] \tag{5.4}$$

The corresponding mean kinetic energy is:

$$\langle E_K \rangle_H = \frac{\bar{h}^2}{2m_H}\left(2\sigma^2(\widehat{t}) + \sigma^2(\widehat{z})\right) \ , \tag{5.5}$$

where $\sigma(\widehat{t})$ and $\sigma(\widehat{z})$ define the widths of two Gaussian momentum distributions, perpendicular and along the hydrogen bond, respectively [20]. In the special case of a single isotropic Gaussian momentum distribution $\sigma(\widehat{t}) = \sigma(\widehat{z})$.

A non Gaussian model for $J(y)$ has also been considered, i.e. a general series expansion such as the Gram-Charlier series, involving Hermite polynomials, $H_n(x)$ [22]. In the case of a liquid, where the average distribution of wave vectors is isotropic, the general expansion of a symmetric longitudinal momentum distribution yields the form [20, 22]:

$$J(y) = \frac{\exp^{-\frac{y^2}{2\sigma^2}}}{\sqrt{2\pi\sigma^2}} \sum_n \frac{a_n}{2^{2n}n!} H_{2n}\left(\frac{y}{\sqrt{2}\sigma}\right) \tag{5.6}$$

Final State Effects can also be incorporated by properly inserting $H_3(\frac{y}{\sqrt{2}\sigma})$ and $H_4(\frac{y}{\sqrt{2}\sigma})$ polynomials.

This model, recently used to describe the DINS response function from liquid water in bulk and confined geometry [11, 20], provides at present the most satisfactory physical description of the proton momentum distribution. The following sections report results from the fits of the experimental data, in both RD and RF configurations, using the different models introduced above.

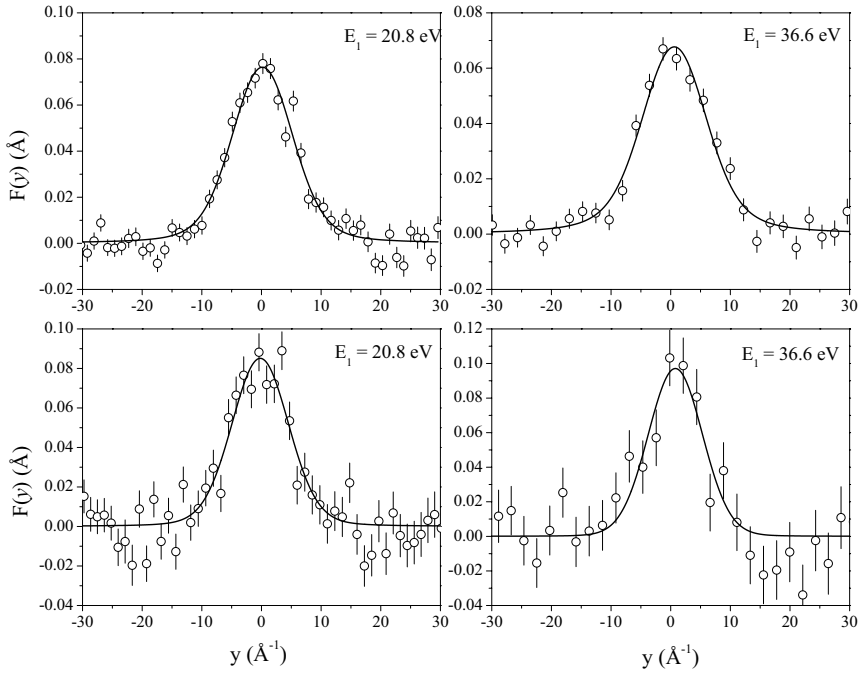

Figure 12. Proton experimental response functions, $F(y)$, and results from the fits obtained using an isotropic Gaussian model for $J(y)$, of H_2O sample at [p=1 bar, T=293 K] in a) Al container upper panel (left panel, $E_1 = 20.8$ eV, right $E_1 = 36.6$ eV) and b) TiZr container (lower panel, left $E_1 = 20.8$ eV, right $E_1 = 36.6$ eV).

5.1 Proton mean kinetic energy in H_2O at [1 bar, 293 K]

At this thermodynamic condition six experimental proton response $F(y)$ functions recorded in the RD configuration were in principle available, three from Al and three from TiZr sample containers, respectively. However, due to the contamination of the first recoil peaks by the background contributions discussed in section 1, only four $F(y)$ functions were included in the present analysis. These functions, fitted using the isotropic Gaussian model for $J(y)$, yielded the value $\sigma_y = (4.42 \pm 0.18)$ Å^{-1} which corresponds to a value for the mean kinetic energy $\langle E_K \rangle = (122 \pm 10)$ meV. An example of these results is shown in figure 12 which shows experimental and fitted response functions from water in Al (upper panels) and TiZr sample containers (lower panels). The experimental response functions have also been fitted using the anisotropic Gaussian model and non Gaussian model for $J(y)$, introduced in equations (5.4) and (5.6). These yielded the results summarized in table 4. The table also reports results obtained from DINS data recorded with VESUVIO operating in RF configuration at the same [p,T] conditions [21].

5.2 Proton mean kinetic energy in H_2O at [100 bar, 423 K]

At this thermodynamic condition three experimental proton response $F(y)$ functions recorded in the RD configuration were available but only two were included in the present analysis because of background contamination of the first recoil peak. These functions, fitted using the isotropic Gaussian model for $J(y)$, provided a value of $\sigma_y = (4.7 \pm 0.25)$ Å^{-1}, corresponding to a value

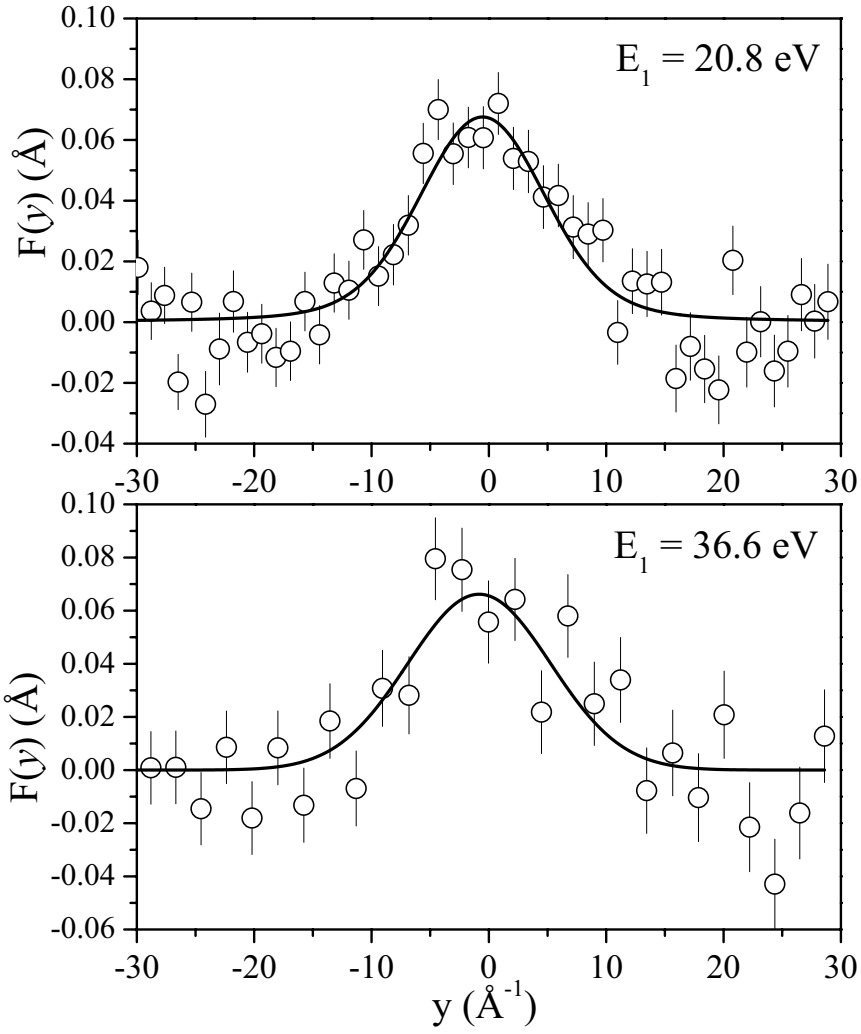

Figure 13. Proton experimental response functions, $F(y)$, and results from the fits obtained using an isotropic Gaussian model for $J(y)$, of H_2O sample at [p =100 bar, T =423 K], in TiZr container (top panel $E_1 = 20.8$ eV, bottom panel $E_1 = 36.6$ eV).

for the mean kinetic energy $\langle E_K \rangle = (137 \pm 16)$ meV. Figure 13 shows the experimental response functions and the corresponding fitted functions.

The anisotropic Gaussian model and non Gaussian model for $J(y)$, have also been fitted to the data, and results of these fits are also reported in table 4, together with values obtained for the analysis of DINS data recorded in the RF configuration [21].

6. Discussion

Although previous works indicate that the proton dynamics in water is best reproduced by the non Gaussian model [11] it is of some interest to compare the different $J(y)$ models used for the fit of the experimental $F(y)$ functions. The upper plot of figure 14 shows the $J(y)$ functions on a linear scale, while in the lower plot, in order to highlight the behavior of the different lineshapes, the response

Sample	$\langle E_k^{\mathbf{RD}} \rangle$ [meV]	$\langle E_k^{\mathbf{RF}} \rangle$ [meV]
Simple Gaussian $J(y)$		
H_2O [1 bar, 293 K]	122 ± 10	124 ± 3
H_2O [100 bar, 423 K]	137 ± 16	129 ± 5
Spherically averaged $J(y)$		
H_2O [1 bar, 293 K]	144 ± 15	147 ± 8
H_2O [100 bar, 423 K]	168 ± 16	156 ± 13
Gram-Charlier expanded $J(y)$		
H_2O [1 bar, 293 K]	149 ± 12	144 ± 3
H_2O [100 bar, 423 K]	161 ± 8	156 ± 6

Table 4. Summary of the $\langle E_K \rangle$ values obtained from RD and RF measurements employing different forms for $J(y)$.

functions are plotted on a *log* scale for $y > 10$ Å^{-1}. The differences in relative areas varies between 1% and 20%. The statistical uncertainty in the y region around 10 Å^{-1} is about 25% for the $F_2(y)$, while the differences among the $J(y)$ are about 5%-10%. Thus an improvement in statistical accuracy by a factor 5 is needed in order to discriminate between the models. The differences found for the $\langle E_K \rangle$ values obtained employing the fitting models mentioned in the previous section, have been already observed in the analysis of $J(y)$ in molecular systems such as H_2S [18] and H_2O (both in subcritical and supercritical thermodynamical conditions) [20, 23]. In the former case an approach based on equation (5.4) was employed and appreciable differences were found with respect to a simple Gaussian approach. In the H_2O case the employment of spherical averaged Gaussian (equation (5.4)) and Gram-Charlier expanded $J(y)$ (equation (5.6)) both pointed out the inadequacy of the simple Gaussian lineshape in describing the proton momentum distribution. In both cases the high momentum tails of the non Gaussian lineshapes discussed above (see figure 14), result in a larger second moment of $J(y)$ and thus in a higher values of the proton mean kinetic energy (see equation (4.9)).

For the $F_3(y)$ (E_1=36.6 eV) the statistical uncertainty, in the same y region, is as large as 50% so that a factor of 10 improvement in accuracy would be needed. Note that this is a conservative requirement since it refers to the analysis of a single resonance. The simultaneous analysis of several resonances is a more sensitive procedure in order to distinguish among the different models.

In future experiments using the RD configuration a factor of 10 improvement in statistical accuracy will be achieved by 100 times better statistics, i.e. increasing the data accumulation time and building a set of RD detectors covering a larger area. In addition an increase of the signal/background (S/B) ratio by nearly an order of magnitude will be achieved by raising the threshold above 500 keV [7]. In this way it has been shown that it is possible to record recoil peaks above 70 eV final neutron energy [7]. The actual S/B improvement is somewhat sample dependent, but a statistical improvement by a factor 2-3 should be possible if the same experiment presented here was repeated with a higher threshold.

2006 JINST 1 P04001

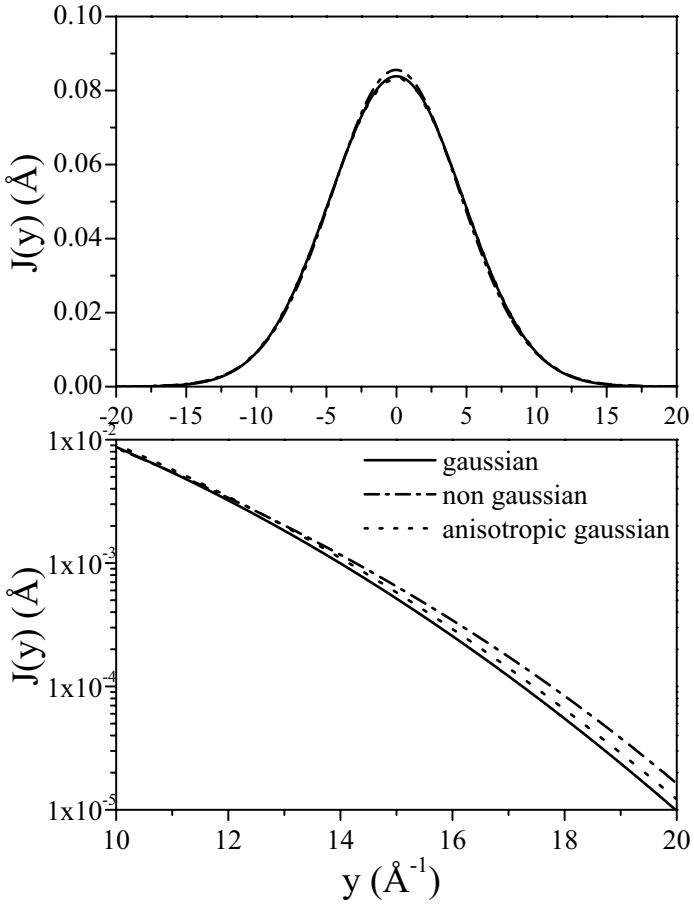

Figure 14. Comparison of different $J(y)$ models. In the upper plot the distributions are plotted in the range -20 Å^{-1} — 20 Å^{-1} on a linear scale; in the lower panel the same distributions are plotted in the $y > 10$ Å^{-1} region and on a log scale to show the differences in the tail region.

The statistical uncertainty in the measurement is mainly due to background and it would pay off if efficient means for background rejection could be devised. Use of γ/neutron shields around the RD bank can always be considered but this would mainly act against the environmental background; sample background would be less affected or it could even get worse because of multiple γ/neutron interactions in the shield. Another approach is coincidence techniques. The γ cascade following resonant neutron absorption has typically a multiplicity of 2-3; simultaneous detection events in pairs of YAP detectors facing the same resonance foil would provide a coincidence measurement of the neutron absorption with much improved background rejection. This approach was tested in a recent experiment where a pair of YAP scintillators was placed in sandwich geometry on either side of a ^{238}U analyzer foil. The scintillators were 6 mm thick and light collection was from the side via a reflecting light guide. With this detector arrangement the amount of material intercepted by the scattered neutrons before being absorbed by the foil amounts to a 6 mm thick YAP slab plus 1 mm Al housing. The gap between ^{238}U foil and planar YAP detectors was about 2 mm. The YAP areas matched the foil area being 2150 mm^2. This "sandwich" RD was used at a

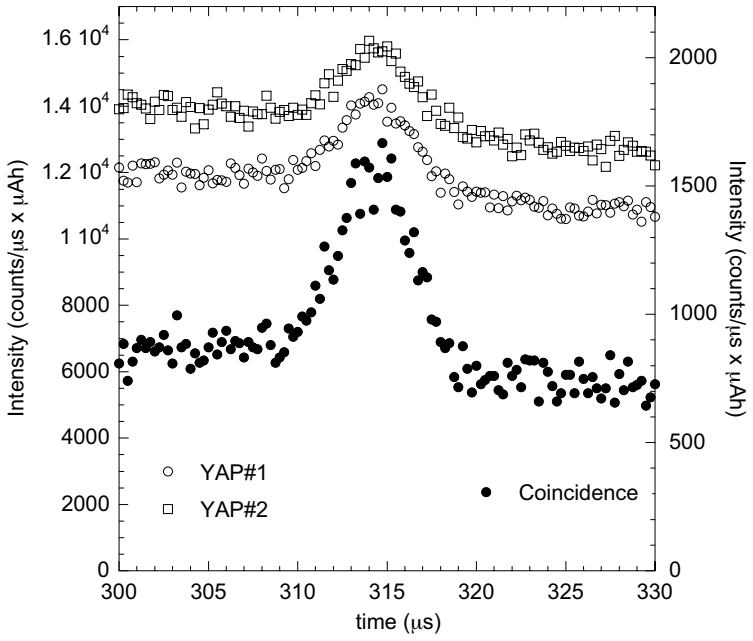

Figure 15. TOF spectra for a Pb sample and the RD coincidence set up described in the text. The coincidence spectrum (full symbols, right hand scale) has a signal/background ratio that is 5 times better than in the individual YAP spectra (empty symbols, left hand scale).

scattering angle of 30°. Shown in figure 15 are the TOF spectra collected from a Pb sample by the YAP detectors individually (empty symbols) and in coincidence (full symbols). The improvement in signal/background ratio is significant (a factor 5 as measured by the ratio of the intensities at the resonance peak) but comes at a price of a drop in intensity by a factor 10. This confirms the expectation that a coincidence approach would only be practical under measurement conditions where the signal intensity is large, which is not normally the case on VESUVIO.

An alternative approach for background rejection is to perform measurements with different foil combinations. In the RF configuration the "double difference" method entails the weighted combination of three measurements without analyzer foil, with a thin foil and with a thick foil [14]. In this way the background effect is reduced and, especially, the Lorentzian tails contribution to the instrument response is almost suppressed, which provides improved signal quality in the tail of the recoil peaks. A somewhat similar approach can be considered in the RD configuration by placing a second analyzer foil in the path between the sample and the γ detector. This method is practical provided there is enough room in the secondary neutron flight path for inserting a second foil at sufficient distance from the RD.

An important advantage of the RD configuration over the RF configuration is the extended range of momentum and energy transfers. This can be argued by considering figure 16 where four $S(\vartheta,\omega)$, corresponding to the first four H recoil peaks for the case of H_2O in the Al container are shown. Each $S(\vartheta,\omega)$ peak is fitted with a Gaussian function (full line) in order to determine the recoil energy $\hbar\omega_r$. The fitted recoil energies, $\hbar\omega_{(r,i)}$, are $\hbar\omega_{(r,1)} \simeq 1.7\,\text{eV}$, $\hbar\omega_{(r,2)} \simeq 5.5\,\text{eV}$, $\hbar\omega_{(r,3)} \simeq 10\,\text{eV}$ and $\hbar\omega_{(r,4)} \simeq 20\,\text{eV}$. Note the different number of experimental points in each peak:

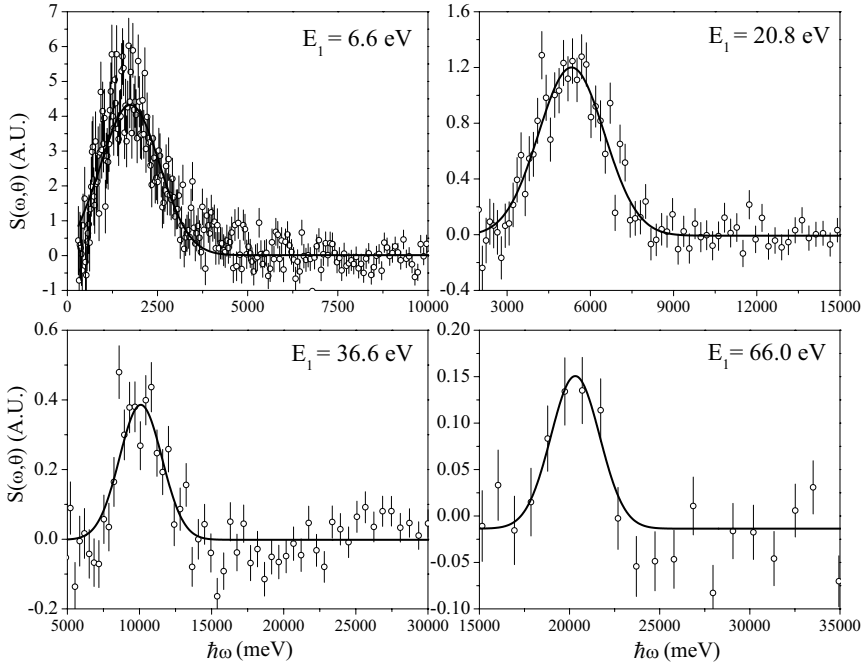

Figure 16. $S(\vartheta,\omega)$ functions for $2\vartheta = 26.7^\circ$ and final neutron energies of about 6.67 eV, 20.8 eV, 36.6 eV and 66.0 eV. The continuous lines are fitted Gaussians.

this is due to the non linear relationship between time and energy, so that the lower the TOF the wider the sampled energy interval corresponding to a given fixed time bin.

As already mentioned in section 4, the Impulse Approximation is strictly valid only in the limit $(q,\omega) \rightarrow \infty$. For finite values of the wave vector and energy transfer a final state effect (FSE) correction should be applied to the $J(y)$, but the correction becomes vanishingly small for increasing values of q and ω. This is illustrated in figure 17 which shows a $J(y)$ obtained through a non Gaussian fit (Gram-Charlier expansion) where $H_3(x)$ and $H_4(x)$ polynomials have been inserted to account for the FSE corrections. The dashed line in each panel shows the FSE component $[J_{\rm FSE}(y,q) - J(y,q)]$. It can be noticed that for the lower panel (E_1 = 36.6 eV and q_p = 69 Å^{-1}, q_p being the value of q at the recoil peak) the effect of the final state interactions provides a smaller contribution as compared to the one in the upper plot (E_1 20.8 eV and q_p = 52 Å^{-1}). As already pointed out, the RD configuration is capable of detecting scattered neutrons well above 10 eV, which is the RF limit. In the present experiment the RD spectra at 2ϑ = 27° were analyzed up to 36.6 eV final neutron energy and these 2ϑ and E_1 values were used in figure 17. However at least the 66.0 eV resonance will be accessible under optimal experimental conditions allowing to extend the (q,ω) range even further. Furthermore since q increases with increasing scattering angle, for a fixed final neutron energy, it can be argued that the FSE contributions will be so low in a complete RD array covering an extended angular range that it should be possible to add the $F(y)'$s at fixed final energy recorded at different angles. This is a simplification in the analysis meaning that the statistical accuracy needed to discriminate among the different models could be achieved by adding measurements from different detectors no matter where they are placed. Quantitatively,

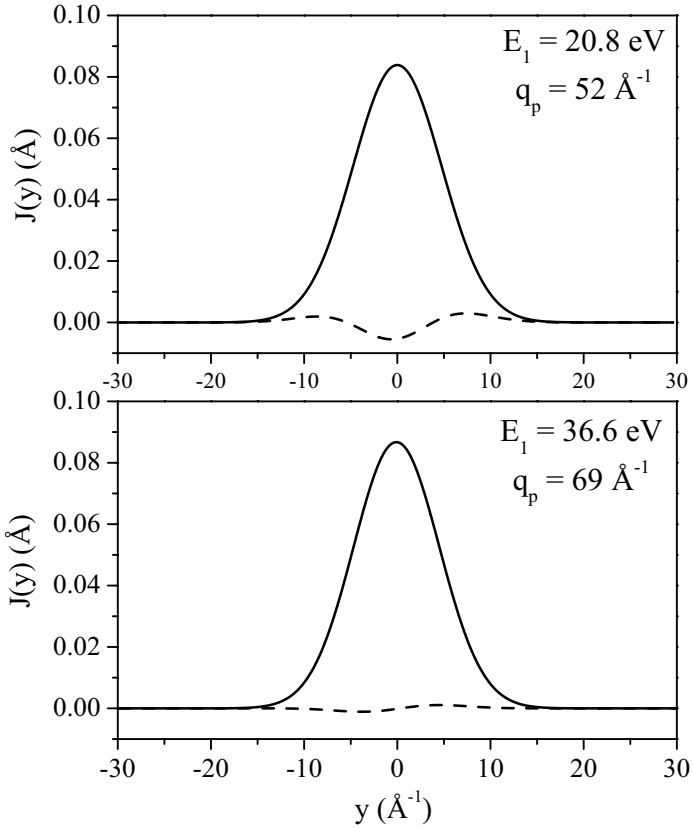

Figure 17. Longitudinal Compton profiles (full lines) corresponding to final energies of 20.8 eV (upper plot) and 36.6 eV (lower plot) obtained through equation (5.6) where $H_3(\frac{y}{\sqrt{2}\sigma})$ and $H_4(\frac{y}{\sqrt{2}\sigma})$ polynomials have been inserted to account for FSE corrections. The dashed line in each panel represents the difference ($J_{\rm FSE}(y)$ - $J(y)$). q_p is the wave vector transfer value calculated at the proton recoil peak $y = 0$.

the maximum value of q_p accessed by the ^{6}Li-glass detectors in the present experiment is about 118 Å^{-1} (for the detectors at about 68°) corresponding to $\bar{\hbar}\omega_r \simeq 29$ eV, which is comparable to the values obtained considering a final neutron energy of 66.0 eV (fourth ^{238}U resonance) which gives $q_p \simeq 90$ Å^{-1} and $\bar{\hbar}\omega_r \simeq 20$ eV, but at a scattering angle of 27°. At E_1 = 66.0 eV and $2\vartheta = 70°$ $q_p \simeq$ 220 Å^{-1} and $\bar{\hbar}\omega_r \simeq 100$ eV. In the end this means that an optimized RD array will have a better statistics, will provide access to a broader kinematic range than possible with the RF configuration, with a corresponding reduced sensitivity to systematic (FSE) effects and improved overall quality of the measurements.

7. Conclusions

Deep Inelastic Neutron Scattering measurements on liquid water have been performed at the VESUVIO spectrometer using the Resonance Detector configuration. The experimental response functions have been analyzed yielding values of the mean proton kinetic energy in agreement with parallel measurements using the Resonance Filter configuration, thus demonstrating the reliability of the RD approach even in a case where the RD measurement conditions were not optimal. Anal-

ysis of the DINS experimental data recorded in RF configuration ([21] and table 4) provides values of $\langle E_K \rangle$ with better statistics as compared to DINS measurements in RD configuration. However it has to be stressed that in the former measurements, DINS spectra were recorded by 32 ^{6}Li-glass detectors whereas in the latter only a single YAP scintillator was available. Furthermore the YAP detector size was six times smaller than a single ^{6}Li-glass detector, with an overall detection area in the RF configuration about 200 times larger than in the RD configuration.

The projected performance of an array of RD detectors optimized for DINS measurements is encouraging in terms of reduced sensitivity to systematic effects and improved overall quality of the measurements. The data analysis procedure employed in the present experiment leads to results which are consistent with those obtained on DINS measurements in the RF configurations. We thus envisage an extended use of RD banks optimized for DINS measurements as part of imminent and future upgrades of the VESUVIO detector system.

Acknowledgments

We acknowledge Dr. J. Mayers and Dr. D. Colognesi for stimulating discussions and suggestions. We acknowledge the financial support of the Consiglio Nazionale delle Ricerche (CNR)-Italy within the CNR-CCLRC agreement.

References

[1] H. Rauh and N. Watanabe, *Nucl. Instrum. Meth.* **228** (1984) 147;
N. Watanabe 1984 *Proc. of the 1984 Workshop on High Energy Excitations in Condensed Matter (Los Alamos)* Vol 1 (**LA-10227-C**).

[2] D.R. Allen, E.W.J. Mitchell and R.N. Sinclair, *J. Phys. E: Sci. Instr.* **13** (1980) 639;
J.M. Carpenter, N. Watanabe, S. Ikeda, Y. Masuda, S. Sato and H. Rauh *Physica* **B 120** (1983) 126.

[3] C. Andreani, A. Pietropaolo, R. Senesi, G. Gorini, M. Tardocchi, A. Bracco, N. Rhodes and E. Schooneveld, *Nucl. Instrum. Meth.* **A 481** (2002) 509.

[4] M. Tardocchi, A. Pietropaolo, C. Andreani, A. Bracco, A. D'Angelo, G. Gorini, S. Imberti, R. Senesi, N.J. Rhodes and E.M. Schooneveld *Nucl. Instrum. Meth.* **526** (2004) 477.

[5] R. Senesi, C. Andreani, Z. Bowden, D. Colognesi, E. Degiorgi, A.L. Fielding, J. Mayers, M. Nardone, J. Norris, M. Praitano, N.J. Rhodes, W.G. Stirling, J. Tomkinson and C. Uden, *Physica* **B 276-278** (2000) S189.

[6] C. Andreani, A. D'Angelo, G. Gorini, S. Imberti, A. Pietropaolo, N.J. Rhodes, E.M. Schooneveld, R. Senesi and M. Tardocchi, *Appl. Phys. A* **78** (2003) 903.

[7] M. Tardocchi and G. Gorini, A. Pietropaolo, C. Andreani and R. Senesi, N.J. Rhodes and E.M. Schooneveld *Rev. Sci. Instrum.* **75** (2004) 4880.

[8] A.C. Evans , J. Mayers, D.N. Timms and M.J. Cooper *Z. Naturforsch A Phys. Sci.* **A 48** (1993) 425;
R.J. Newport, M.P. Paoli, V.T. Pugh, R.N. Sinclair, A.D. Taylor and W.G. Williams *Proc. of the eighth Meeting of the International Collaboration on Advanced Neutron Sources* (RAL-85-110 Rutherford Appleton Laboratory) 1985 p 562.

[9] E. Perelli-Cippo, G. Gorini, M. Tardocchi, C. Andreani, A. Pietropaolo, R. Senesi, N.J. Rhodes and E.M. Schooneveld *J. Phys.: Cond. Matt.*, submitted for publication;

[10] A.L. Fielding and J. Mayers, *Nucl. Instrum. Meth.* **A 480** (2002) 680.

[11] C. Andreani, D. Colognesi, J. Mayers, G.F. Reiter and R. Senesi, *Adv. Phys.* **54** (2005) 377.

[12] G. Watson, *J. Phys.: Condens. Matter* **8** (1996) 5955;
E. Pace, G. Salmé and G.B. West *Phys. Lett.* **B 273** (1991) 205.

[13] S.W. Lovesey, *Theory of neutron scattering from condensed matter*, 3rd ed. Oxford University Press, 1987.

[14] C. Andreani, D. Colognesi, E. Degiorgi, A. Filabozzi, M. Nardone, E. Pace, A. Pietropaolo and R. Senesi *Nucl. Instrum. Meth.* **A 497** (2003) 535;
C.G. Windsor, *Pulsed Neutron Scattering*, Taylor & Francis Ltd, 1981.

[15] V.F. Sears *Phys. Rev.* **B 30** (1984) 44.

[16] H.R. Glyde *Phys. Rev.* **B 50** (1994) 6726.

[17] F. James, *MINUIT minimisation package: reference manual*, Geneva, CERN Program Library, 1999.

[18] C. Andreani, E. Degiorgi, R. Senesi, F. Cilloco, D. Colognesi, J. Mayers, M. Nardone and E. Pace, *J. Chem. Phys.* **114** (2001) 387.

[19] C. Andreani, D. Colognesi, E. Degiorgi and M.A. Ricci, *J. Chem. Phys.* **115** (2001)11243;

[20] G.F. Reiter, J.C. Li, J. Mayers, T. Abdul-Redah, P. Platzman 2004 *Bras. J. Phys.* **34** 142;

[21] A. Pietropaolo, *Research and development of γ detectors for neutron scattering at electron Volt energies on the VESUVIO spectrometer*, PhD Thesis, Roma: Universitá degli Studi di Roma “Tor Vergata”, 2004.

[22] V.F. Sears, *Phys. Rev.* **185** (1969) 200.

[23] C. Andreani, D. Colognesi, J. Mayers, G.F. Reiter and R. Senesi, *Adv. Phys.* **54** (2006) 377.

2006 JINST 1 P04001